

1

2 **Imaging the Hydrothermal System of Kirishima Volcanic Complex, Japan with L-band**

3

**InSAR Time Series**

4 **Zhang Yunjun<sup>1,†</sup>, Falk Amelung<sup>1</sup>, and Yosuke Aoki<sup>2</sup>**

5 <sup>1</sup>Rosentiel School of Marine and Atmospheric Science, University of Miami, Miami, FL, USA.

6 <sup>2</sup>Earthquake Research Institute, University of Tokyo, Tokyo, Japan.

7 <sup>†</sup>Now at Seismological Laboratory, California Institute of Technology, Pasadena, CA, USA.

8 Corresponding author: Z. Yunjun ([yunjunzgeo@gmail.com](mailto:yunjunzgeo@gmail.com))

9 **Key Points:**

- 10
- Shinmoe-dake hydrothermal system deflated during the 2008-2010 eruptions, then was replaced by a magmatic body during the 2011 eruption.
- 11
- Persistent inflation at the Iwo-yama crater during 2014-2019 is driven by liquid-gas two-phase water boiling.
- 12
- Precursory expansion of Iwo-yama's southern and western vents after December 2017 is driven by the upward migration of magmatic fluid.
- 13
- 14
- 15

**16 Abstract**

17 We present deformation measurements of the Kirishima volcanic complex from ALOS and  
18 ALOS-2 Interferometric Synthetic Aperture Radar (InSAR) time-series during 2006-2019.  
19 Shinmoe-dake deflated ~6 cm during the 2008-2010 phreatic eruptions and inflated ~5 cm prior  
20 to the 2017 magmatic eruption. Iwo-yama inflated ~19 cm within the crater since January 2015  
21 and ~7 cm around the southern and western vents since four months before the 2018 eruption.  
22 These deformations can be modeled as ellipsoids at ~700 m depth beneath Shinmoe-dake and as  
23 a sphere on top of an ellipsoid at ~130 and ~340 m depths beneath Iwo-yama. Combining  
24 geodetic, geoelectric, geochemical and petrological analysis, we interpret the hydrothermal  
25 origin of the deflation at Shinmoe-dake and inflation at Iwo-yama; the hydrothermal-magmatic  
26 transition during the 2011 Shinmoe-dake eruption; water-boiling and bottom-up pressurization as  
27 driving mechanisms of the inflation at Iwo-yama. The study highlights the imaging potential of  
28 InSAR time-series on complex hydrothermal systems.

**29 Plain Language Summary**

30 Steam-blast eruptions are driven by the heat of magma interacting with water. Although small in  
31 size, they are very common and unpredictable, making them hazardous. In order to know when  
32 and where these interactions started and how they led to the eruption, we take the Kirishima  
33 volcano group as an example and use 10 years of satellite radar images to measure its ground  
34 surface deformation. We find that Shinmoe-dake fell ~6 cm during the 2008-2010 eruptions,  
35 much earlier than previously thought; while Iwo-yama rose ~7 cm since four months before its  
36 2018 eruption. Combining models from specialized computer code with previous studies from  
37 other disciplines, we explain the fall of Shinmoe-dake and the rise of Iwo-yama are due to the  
38 steam release and water accumulation of water-rich zones at ~700 m and ~340 m depth below

39 the surface, respectively. The water-rich zone of Shinmoe-dake was replaced and filled by  
40 magma during the 2011 eruption. These short-lived, small-size deformations have not been  
41 identified in the region before, nor has the type of deformation in general been studied  
42 extensively worldwide. Future volcano monitoring efforts should take this into account on a  
43 regular basis.

## 44 **1 Introduction**

45 Phreatic eruptions are among the most common but also among the most unpredictable  
46 volcanic phenomena, making them hazardous despite the relatively small scale. Unlike magmatic  
47 eruptions driven by magma migration, volatile exsolution and crystallization, phreatic eruptions  
48 are driven by broadly defined hydrothermal processes, such as interactions among water, rocks  
49 and magmatic heat and gas, similar to geyser-like mechanisms but more violent with the  
50 expulsion of rocks and mud, usually without juvenile material (Germanovich & Lowell, 1995;  
51 Muffler et al., 1971; Stix & Moor, 2018). Many of the largest volcanic eruptions started with  
52 phreatic events, e.g. the 1980 Mt. St. Helens eruption (Christiansen et al., 1982) and the 1991  
53 Pinatubo eruption (Newhall & Punongbayan, 1996), but phreatic eruptions may also occur in  
54 isolation.

55 Geophysical monitoring of phreatic eruptions has been challenging due to their localized  
56 deformation signals with small magnitude and sudden occurrence with few if any precursors  
57 (Kobayashi et al., 2018). Although not as frequently as magmatic processes, ground deformation  
58 associated with hydrothermal processes has been observed in all stages of volcanic eruption  
59 cycles, including the pre-eruptive (Kobayashi et al., 2018; Narita et al., 2020), co-eruptive  
60 (Himematsu et al., 2020), post-eruptive period (Hamling et al., 2016; Nakaboh et al., 2003;

61 Narita & Murakami, 2018) and non-eruptive unrest period (Battaglia et al., 2006; Lu et al., 2002;  
62 Lundgren et al., 2001).

63 Here we report a decade-long Interferometric Synthetic Aperture Radar (InSAR)  
64 deformation time-series of the Kirishima volcanic complex, Japan during 2006-2011 and 2014-  
65 2019, covering the 2008 and 2017 Shinmoe-dake eruptions and the 2018 Iwo-yama eruption. We  
66 estimate the location, geometry and volume change of the pressure sources and combine them  
67 with previous observations from resistivity, geochemistry and petrology to a new model for the  
68 shallow plumbing system of the central Kirishima volcanoes.

## 69 **2 Geological Setting**

70 The Kirishima volcanic complex (Japanese for foggy mountain) is located in southern  
71 Kyushu, where the Phillipine Sea Plate is subducted beneath the Amurian Plate (Wallace et al.,  
72 2009). The complex consists of more than 25 craters, cones and lava domes produced by the  
73 southward migration of eruption centers in the last 330 ka (Fig. 1a; Nakada et al., 2013). These  
74 volcanic centers form an elliptical 30 by 20 km northwest-trending zone with younger volcanism  
75 generally in the southeast (Chapman et al., 2009). The most active eruptive centers are Iwo-yama  
76 (Japanese for sulfur peak), Shinmoe-dake and Ohachi (altitudes of 1,313 m, 1,421 m and 1,408  
77 m, respectively). Hydrothermal systems are widely distributed in shallow levels throughout  
78 Kirishima (e.g., Aizawa et al., 2014; Ohba et al., 1997). It has been suggested that the magmatic  
79 system beneath connects at depth with Aira caldera located 20 km to the south (Brothelande et  
80 al., 2018).

81 The 2011 Shinmoe-dake eruption is the first magmatic eruption in the complex since its  
82 1716-17 eruption. Other eruptions at Shinmoe-dake in 1822, 1959 and 1991 are phreatic (Imura  
83 & Kobayashi, 1991). Iwo-yama, the youngest volcanic center, was formed in the 16<sup>th</sup>-17<sup>th</sup>

84 century and had a phreatic eruption in 1768 (Tajima et al., 2014). Ohachi had a series of  
85 eruptions between 1880 and 1923 (GVP, 2013).

### 86 **3 The 2008-2019 Activity**

87 The unrest of Shinmoe-dake started with a substantial increase in seismicity and a rapid  
88 strain change three days before the first phreatic eruption on 22 August 2008 when a lake was  
89 present in the crater (Geshi et al., 2010; Yamazaki et al., 2020). Additional phreatic eruptions  
90 occurred from March to July 2010 (solid blue line/box in Fig. 1i). The 2011 eruption started with  
91 a phreatomagmatic eruption on 19 January and three sub-Plinian eruptions on 26-27 January,  
92 followed by stages of lava extrusion, Vulcanian and phreatomagmatic eruptions until September  
93 (Nakada et al., 2013). Shinmoe-dake had new magmatic eruptions on 11-17 October 2017 and 1  
94 March to 27 June 2018 (solid orange line/box in Fig. 1i; GVP, 2013).

95 In December 2009, more than a year after the first phreatic eruption, GPS and InSAR  
96 data showed inflation over the western flank of the volcanic complex that was attributed to an  
97 inflating pressure source beneath Ebino-dake at ~10 km depth (dashed circle in Fig. 1a; Fig. 1h;  
98 Nakao et al., 2013; Miyagi et al., 2013). Rapid strain change is reported three days before this  
99 inflation (Yamazaki et al., 2020). The source deflated during the climactic phase of the 2011  
100 Shinmoe-dake eruption and re-inflated until November 2011 (Fig. 1h; Nakao et al., 2013; Ueda  
101 et al., 2013).

102 About an hour and a half prior to the first sub-Plinian eruption tiltmeter and broadband  
103 seismometer recorded localized inflation near the crater suggesting a shallow pressure source  
104 (Takeo et al., 2013). In the following two weeks, this source underwent a sequence of inflation-  
105 deflation cycles during the sub-Plinian, lava extrusion and Vulcanian stages. The deformation  
106 signals, synchronized with volcanic tremors or long-period events, were attributed to the

107 pressurization of a shallow conduit beneath the crater (Nakamichi et al., 2013; Takeo et al.,  
108 2013). Localized deflation and inflation patterns were also observed from November 2011 to  
109 May 2013 and prior to the 2017 magmatic eruption (Miyagi et al., 2014; Morishita & Kobayashi,  
110 2018).

111 The unrest of Iwo-yama started with an increase in seismicity in December 2013,  
112 followed by tremors in August 2014, thermal anomalies and weak fumarolic activity since  
113 December 2015, a steam blowout event on 27 April 2017 at the crater and small phreatic  
114 eruptions on 19 and 20 April 2018 at two newly appeared vents on the southern and western side  
115 of the crater with plume heights of 100-200 m (Tajima et al., 2020; dashed blue lines in Fig. 1g-  
116 i). Localized pre-eruptive inflation suggests a very shallow pressure source at 150 m depth  
117 beneath the crater (Narita et al., 2020). Fumarolic activity and mud ejection continued from the  
118 southern and western vents as of December 2019 (JMA, 2019).

#### 119 **4 InSAR Data and Method**

120 We use 2006-2011 ALOS (ascending track 424 and descending track 73) and 2014-2019  
121 ALOS-2 (ascending track 131 and descending track 23) L-band stripmap SAR imagery to form  
122 small temporal and spatial baseline interferograms (see Fig. S1 and Table S1 for detailed  
123 configurations). We remove the topographic phase using the Digital Elevation Model (DEM)  
124 released by Geospatial Information Authority of Japan (GSI, 0.4 arc second, ~10 m) and unwrap  
125 the phase using the minimum cost flow method (Chen & Zebker, 2001). Ionospheric delays are  
126 not corrected.

127 We use the stripmap stack processor (Fattahi et al., 2017) of the ISCE software (Rosen et  
128 al., 2012) for interferogram processing and the Miami InSAR time-series software in Python  
129 (MintPy) for time series analysis (Yunjun et al., 2019). We exclude low-coherence

130 interferograms using coherence-based network modification with a custom area of interest  
131 around Shinmoe-dake (black empty square in Fig. S2) for the average coherence calculation and  
132 thresholds of 0.7 for ALOS descending track 73 and 0.8 for the others. We correct for the  
133 stratified tropospheric delay using the ERA-5 atmospheric reanalysis model (Copernicus Climate  
134 Change Service, 2017; Jolivet et al., 2011), for long spatial-wavelength phase components by  
135 removing linear phase ramps from all acquisitions and for topographic residuals due to the DEM  
136 error (Fattahi & Amelung, 2013; Fig. S3). We use a temporal coherence threshold of 0.8 to  
137 eliminate unreliable pixels. Noisy acquisitions with residual phase root mean squares larger than  
138 the predefined cutoff (1 and 2 median absolute deviations for ALOS and ALOS-2, respectively)  
139 are excluded during the estimation of topographic residual and average velocity (empty circles in  
140 Fig. 1g; Fig. S4).

141 To obtain the optimal InSAR measurement for time periods of interest (Fig. 1d-f), we  
142 apply two extra steps in addition to the routine MintPy workflow (Fig. S5-S8). First, to maximize  
143 the number of reliable pixels we exclude interferograms with acquisitions after the 2011 and  
144 2017 eruptions, which are decorrelated by local processes inside the crater and/or by the newly  
145 deposited ash nearby (Fig. S9-S10). Second, to mitigate residual atmospheric turbulence we  
146 estimate the linear line-of-sight (LOS) velocities for the time periods of interest and convert them  
147 to cumulative displacements instead of using the differential displacement between two  
148 acquisitions (see Fig. S11 for a comparison).

149 Within the Shinmoe-dake crater, lava domes from the 2011 and 2017 eruptions dominate  
150 the topography change (DEM error) since the DEM generation before 2011. We use the locally  
151 referenced DEM errors from ALOS-2 ascending and descending InSAR time-series between the  
152 2011 and 2017 eruptions to measure the thickness and volume of the lava dome extruded from

153 the 2011 eruption (see Fig. S12 for details), providing an alternative approach to the SAR  
154 intensity simulation and the single-pass SAR interferometry (Ozawa & Kozono, 2013; Shimono  
155 et al., 2011).

## 156 **5 Results**

157 We obtain the quasi-vertical displacements from ascending and descending data (Wright  
158 et al., 2004) during 2006-2019 to examine the deformation at the Kirishima volcanic complex  
159 and find five distinct spatial patterns: three at Shinmoe-dake and two at Iwo-yama during three  
160 different time periods (Fig. 1d-f; Fig. S13-S15). Shinmoe-dake deflated  $\sim 6$  cm between the  
161 2008-2010 phreatic eruptions (blue colors in Fig. 1d), inflated  $\sim 5$  cm prior to the 2017 magmatic  
162 eruption (yellow-red colors in Fig. 1e) and has been deflating since the end of the 2018  
163 magmatic eruption (Fig. 1f). Iwo-yama did not show any signal before 2011 (Fig. 1d) but has  
164 been inflating since at least January 2015. The deformation is localized and concentrated on the  
165 crater area during 2015-2017 (Fig. 1e), then expanded to a larger area in December 2017 (Fig.  
166 1f), four months prior to the April 2018 phreatic eruption (dashed blue line in Fig. 1g) when new  
167 vents appeared on the southern and western side of the crater.

168 The LOS displacement time-series show temporal details (Fig. 1g). At Shinmoe-dake, the  
169 eastern crater rim (point A) shows no noticeable deformation prior to the 2008 phreatic eruption  
170 (solid blue line) and  $\sim 6$  cm of linear LOS decrease (subsidence) between the 2008-2010 phreatic  
171 eruptions; the western crater rim (point B) shows  $\sim 4$  cm of LOS increase (uplift) prior to the  
172 2017 magmatic eruption (solid orange line) and a net  $\sim 4$  cm of near-linear LOS decrease after  
173 the 2018 magmatic eruption. At Iwo-yama, the crater (point C) shows  $\sim 19$  cm of near-linear  
174 LOS increase during 2014-2019 while the southern and western vents (points S and W) show no  
175 significant displacement before December 2017 but  $\sim 5$  and  $\sim 7$  cm of LOS increases afterward.

176 This horizontal expansion since December 2017 coincides with the increased seismic activity  
177 (Fig. 1i). Since the end of 2018, Iwo-yama shows no noticeable displacement except for the  
178 vicinity of its western vent where linear LOS increase continues until August 2019.

179 Note that the relatively strong localized inflation on the western summit flank of  
180 Shinmoe-dake prior to the 2017 eruption (Fig. 1e) is likely related to a potentially partially  
181 solidified fissure from which the previous 2008-2010 eruptions occurred (Geshi et al., 2010). We  
182 do not interpret the pre-/co-/post-eruptive deformation of the 2018 Shinmoe-dake eruption as  
183 shown in the GPS baseline change (Fig. 1h) due to the overlap with the erupted ash/tephra from  
184 the 2017 eruption (Fig. 1f; Fig. S7-S8 and S16). Similar ash/tephra deposits are also observed  
185 during the 2011 eruption from phase (Fig. S17) and coherence measurement (Jung et al., 2016).

## 186 **6 Modeling**

187 We use geophysical inverse models to constrain sources of deformation at Shinmoe-dake  
188 during 2008-2010 and 2015-2017 and at Iwo-yama during 2015-2017 and 2017-2019. We  
189 assume an isotropic elastic half-space and use the vectorized finite compound dislocation models  
190 (CDM), composed of three mutually orthogonal rectangular dislocations (with semi-axes  
191  $a_x, a_y, a_z$ ) with uniform opening and full rotational degrees of freedom (Nikkhoo et al., 2016;  
192 see also Beauducel et al., 2020). The CDM model represents a generic ellipsoid eliminating the  
193 need to pre-specify the source geometry such as sphere or sill. We substitute two semi-axes  
194  $a_y, a_z$  of the CDM with their dimensionless ratios to  $a_x$  as  $a_y/a_x$  and  $a_z/a_x$ , for easier  
195 constraints on the source shape if needed. For Shinmoe-dake during 2015-2017 we fixed the  
196 shape and orientation of the CDM due to the lack of near-field observations (we eliminated data  
197 points inside the crater affected by local processes). For Iwo-yama during 2017-2019 we use two  
198 CDMs and fix one of them with the geometry and location inferred from the previous 2015-2017

199 period. Although hydrothermal processes deform the ground in a thermo-poro-elastic fashion,  
200 simple elastic models are well suited to infer the source geometric features for deformation from  
201 distinct episodic unrest where poroelastic response dominates (Fournier & Chardot, 2012; Lu et  
202 al., 2002). If mechanically weak layers are present the sources will be deeper than estimated here  
203 (Manconi et al., 2007). We use a Poisson's ratio of 0.25.

204 We account for the elevation effect of the topography using the varying-source depth  
205 method (Williams & Wadge, 1998). The height value from GSI DEM is converted from ellipsoid  
206 to geoid (31.2 m difference), which is not negligible considering the shallow depth. To fulfill the  
207 positive depths requirement of the CDM solution, we apply a minimum free surface height  
208 constraint of 1,100 m for Shinmoe-dake and of 1,300 m for Iwo-yama. The impact is negligible  
209 for all models except for Iwo-yama during 2017-2019, where the lower source of the two could  
210 be shallower ( $<56$  m) than estimated here but within the reported 95% confidence intervals  
211 ( $\pm 100$  m; see Table S2 for a detailed evaluation).

212 We jointly invert the ascending and descending InSAR LOS displacement measurements  
213 using the Bayesian approach in GBIS (Bagnardi & Hooper, 2018). We subsample the data using  
214 a gradient-based adaptive quadtree method (Jónsson et al., 2002) in the near field and use  
215 uniform sampling in the far-field (where the signal-to-noise ratio is low; Table S3; Fig. S18-  
216 S19). We account for the data uncertainties using structural functions (Lohman & Simons, 2005;  
217 Table S3). We use uniform prior probability density functions (PDF) bounded by geologically  
218 realistic values. The inversion algorithm samples posterior PDF of source model parameters with  
219 1,000,000 iterations. The optimal (maximum a posteriori probability) parameter value and 95%  
220 confidence intervals are shown in Table S4. All free model parameters converged well except the  
221 semi-axis along the X-axis for Shinmoe-dake during 2015-2017 and the opening of the upper

222 CDM for Iwo-yama during 2017-2019. There are trade-offs between some parameters (see joint  
 223 PDF in Fig. S20-S23) but do not affect the depth and derived volume change.

224 For Shinmoe-dake, the optimal solution for the 2008-2010 deflation is a slightly inclined  
 225 prolate ellipsoid (Fig. 2a-e) beneath the northeastern crater section with the centroid at depth of  
 226  $\sim 620 \pm 50$  m below the summit (black star in Fig. 2c-d). For the 2015-2017 inflation, the optimal  
 227 solution is a sphere beneath the crater center at depth of  $\sim 730 \pm 210$  m below the summit (black  
 228 star in Fig. 2h-i). The estimated cavity volume changes for the two time periods are  $-124 \pm 26 \times$   
 229  $10^3 \text{ m}^3$  and  $146 \pm 95 \times 10^3 \text{ m}^3$ , respectively.

230 For Iwo-yama, the optimal solution for the 2015-2017 inflation is a sphere with  $\sim 70$  m  
 231 semi-axes at depth of  $\sim 130 \pm 10$  m below the summit with an estimated cavity volume increase  
 232 of  $15 \pm 2 \times 10^3 \text{ m}^3$ . The optimal solution for 2017-2019 inflation is two CDMs on top of each  
 233 other: one sphere with fixed parameters from the 2015-2017 period except for a free opening  
 234 bounded by the 95% confidence intervals assuming a constant opening rate and one ellipsoid  
 235 located at depth of  $\sim 340 \pm 100$  m below the summit with elongated dimension along the east-  
 236 west direction. The estimated total cavity volume increase is  $76 \pm 39 \times 10^3 \text{ m}^3$ .

## 237 **7 Discussion**

238 The InSAR time-series deformation provides new insights into the shallow volcanic  
 239 system (within the volcanic edifice) of the central Kirishima volcanoes, in addition to a well-  
 240 established deep source beneath Ebino-dake at  $\sim 10$  km depth below the surface.

### 241 **7.1 Shinmoe-dake: Hydrothermal origin of the 2008-2010 deflation**

242 The deflation between the 2008-2010 phreatic eruptions is of hydrothermal origin, as  
 243 most of the erupted material before March 2010 is hydrothermally altered ( $<1$  vol% of juvenile

244 material; Suzuki et al., 2013). This is consistent with geoelectrical-detected widespread shallow  
245 low-resistivity, water-saturated porous layers (e.g. Aizawa et al., 2014). Furthermore, most of the  
246 deflation occurred before December 2009 when the deep source began to inflate (point A in Fig.  
247 1g).

248 The prolate geometry from geodetic modeling could indicate the depressurization of a  
249 former magmatic conduit. The estimated cavity volume decrease ( $124 \pm 26 \times 10^3 \text{ m}^3$ ) is similar  
250 to the volume of erupted tephra ( $120 \times 10^3 \text{ m}^3$ ; Geshi et al., 2010) from the August 2008  
251 eruption. No noticeable co-eruptive deformation is observed from InSAR (point A in Fig. 1g). A  
252 possible mechanism is that the August 2008 eruption unsealed the system and emptied the  
253 reservoir, which was immediately refilled by hydrothermal fluids; these fluids were released via  
254 steam emission (JMA, 2019) during 2008-2010, resulting in surface subsidence.

## 255 7.2 Shinmoe-dake: Replacement of hydrothermal system by magmatic body

256 The 2015-2017 inflation prior to a magmatic eruption was almost certainly magmatic, as  
257 indicated by the elevated  $\text{SO}_2$  emission higher than the background level since 2011 (JMA,  
258 2019). The inferred depth of 730 m is very similar to 2008-2010 (overlapping PDFs in Fig. 3a).  
259 A similar source depth was also inferred for the Vulcanian stage of the 2011 magmatic eruption  
260 (Takeo et al., 2013) and for November 2011 to May 2013 magma extrusion period (Miyagi et al.,  
261 2014). These depths suggest that the deflation/inflation during the above four periods are from  
262 the same source. Together, the similar geodetic source depths, the appearance and dominance of  
263  $\text{SO}_2$  fluxes and juvenile materials from ash samples suggest that part of the porous rock mass that  
264 acted as a hydrothermal source in 2008-2010 was replaced by a magmatic body during the 2011  
265 eruption and stayed as magmatic since then. This is similar to the 2014-2015 phreatic-magmatic

266 transitions in Turrialba volcano inferred from gas emission data (de Moor et al., 2016) but at a  
 267 much shallower level and transited only once.

### 268 7.3 Iwo-yama: Triple-source hydrothermal system

269 The expanded inflation at Iwo-yama since December 2017 cannot be explained by the  
 270 single source at 130 m depth (very well constrained with a 95% confidence interval of <10 m  
 271 due to the shallow depth and coherent near-/far-field observation). Geodetic modeling suggests  
 272 an extra east-west oriented lay-down cigar-shaped source further down at depth of 340 m (Fig.  
 273 2p-t and 3b) with two sources on top of each other at very shallow depths prior to the eruption.  
 274 Both sources are hydrothermal as evident from the strong fumarolic activity, steam emissions,  
 275 and ejection of mud and hot water since 2014 (JMA, 2019).

276 The upper source at 130 m depth (1180 m a.s.l.) has been inflating since at least January  
 277 2015 (point C in Fig. 1g). There is a minor peak location change during 2016-2018 around the  
 278 Iwo-yama crater (Narita et al., 2020). Geochemical analysis in 2016 shows that the water is  
 279 meteoric (Tajima et al., 2020), suggesting the upward migration of magmatic fluid is not the  
 280 primary direct driver. Geoelectric surveys have resolved a low-resistivity zone at 200-700 m  
 281 depth (Tsukamoto et al., 2018), which is below the upper source thus can not serve as caprocks  
 282 for hydrothermal sealing to support persistent overpressure. The fumarolic temperature has  
 283 continuously been around or above 96 °C (Tajima et al., 2020), which is the water boiling point  
 284 temperature at 1180 m a.s.l. Thus, we conclude that the liquid-gas two-phase boiling of meteoric  
 285 water is the primary driver of the persistent localized inflation around the Iwo-yama crater.

286 The lower source at 340 m depth hosts the southern and western vents and is responsible  
 287 for the April 2018 eruption. Considering 1) the mix of meteoric and magmatic water and the  
 288 sharp increase of SO<sub>2</sub> and H<sub>2</sub> concentrations in fumarolic gas from the geochemical analysis in

289 2018 before the eruption and 2) the observation of days of fluid upwelling just before the 2017  
290 blowout and 2018 eruption (Ohba et al., 2021; Tajima et al., 2020), we interpret the expanded  
291 inflation is driven by the bottom-up pressurization from the upward migration of magmatic fluid.  
292 The magmatic fluid is likely generated by the interaction between local meteoric water and  
293 magmatic vapor rising from the depth (Ohba et al., 2021).

294 Residuals of geodetic modeling show a localized uplift at the western vent after  
295 December 2017 (Fig. S24 and the difference between solid lines and empty circles in Fig. 2t).  
296 The small spatial scale (~150 m in diameter) and the exact same location from ascending and  
297 descending orbits suggest the corresponding pressure source is even shallower than the one at  
298 130 m depth. In total, Iwo-yama hosts a complex hydrothermal system with three tiny reservoirs  
299 at very shallow depths.

#### 300 7.4 Conceptual model of the Kirishima plumbing system

301 The magmatic and hydrothermal plumbing system of the Kirishima volcanic complex is  
302 summarized in Fig. 3c. A deep (~10 km below the surface) magmatic source beneath Ebino-dake  
303 inflated between December 2009 and the 2011 eruption (Fig. S17) and inflated again between  
304 the 2017 and 2018 eruption (Fig. 1h). The shallow source beneath Shinmoe-dake (~700 m below  
305 the summit) was hydrothermally evacuating gas and steam between the 2008-2010 phreatic  
306 eruptions, then turned magmatic during the 2011 eruption and has been accumulating magma  
307 since at least January 2015, feeding the 2017 and 2018 magmatic eruptions. The very shallow  
308 hydrothermal reservoir beneath Iwo-yama (130 m below the summit) has been boiling since at  
309 least January 2015. In December 2017 another slightly deeper hydrothermal reservoir (340 m  
310 below the summit) started accumulating magmatic fluid, feeding the April 2018 phreatic  
311 eruption. These shallow hydrothermal reservoirs beneath Iwo-yama are possibly connected to the

312 subvertical conductor (2-10 km b.s.l.; Aizawa et al., 2014) via magma degassing and  
313 hydrothermal fluid migration (Ohba et al., 2021; Tsukamoto et al., 2018), thus, sharing the same  
314 origin of deep magmatic source with Shinmoe-dake.

## 315 **8 Conclusions**

316 We derived the surface deformation history of the Kirishima volcanic complex during  
317 2006-2011 and 2014-2019 using InSAR time series analysis. Built upon the routine workflow,  
318 we demonstrated that excluding interferograms after destructive eruptions and using average  
319 velocity could increase the spatial coverage of near-field observation and further beat down the  
320 residual tropospheric turbulence after tropospheric correction, to improve the displacement  
321 estimate for time periods of interest. We also described a new approach for lava dome mapping  
322 using DEM errors from time series analysis.

323 Combining geodetic and petrologic data, we identified the hydrothermal reservoir  
324 beneath Shinmoe-dake subsiding after the August 2008 eruption, much earlier than the  
325 previously thought precursory magmatic inflation since December 2009. The compilation of  
326 multiple geodetic studies suggests this hydrothermal reservoir is replaced by a magmatic body  
327 during the 2011 eruption. At Iwo-yama, the deformation time-series reveals a precursory  
328 horizontal expansion for the 2018 eruption. We propose a hydrothermal system with three tiny  
329 reservoirs beneath Iwo-yama at very shallow levels to explain the observed deformation.

330 Combining geodetic, geoelectric and geochemical data, we conclude that the deformation is  
331 driven by liquid-gas two-phase boiling of meteoric water at the upper reservoir and bottom-up  
332 pressurization from upward migration of magmatic water at the lower reservoir. The study  
333 highlights the imaging potential of InSAR time-series for complex hydrothermal systems and the  
334 importance of multidiscipline data for understanding volcanic processes.

335 **Data and Code Availability**

336 The InSAR displacement products and geodetic modeling results are available on Zenodo  
 337 (<https://doi.org/10.5281/zenodo.4661725>, <https://doi.org/10.5281/zenodo.4499238> and  
 338 <https://doi.org/10.5281/zenodo.4499208>). Figures are prepared using GMT (Wessel et al., 2013)  
 339 and Matplotlib (Hunter, 2007) in Jupyter Notebook available on Zenodo  
 340 (<https://doi.org/10.5281/zenodo.4661735>).

341 **Acknowledgments**

342 The ALOS and ALOS-2 data are shared among the PALSAR Interferometry Consortium to  
 343 Study our Evolving Land surface (PIXEL) and provided by JAXA under contract with the  
 344 University of Tokyo. The ownership of SAR data belongs to JAXA and the Ministry of  
 345 Economy Trade and Industry. We thank GSI for the DEM and GPS data, JMA for the earthquake  
 346 data. We thank Jamie Farquharson, Heresh Fattahi, Mehdi Nikkhoo, Piyush Agram and Bhuvan  
 347 Varugu for discussions. This work was supported by NASA Headquarters under the Earth and  
 348 Space Science Fellowship program (Grant No. NNX15AN13H) and National Science  
 349 Foundation's Geophysics program (Grant No. EAR1345129).

350 **References**

351 Aizawa, K., et al. (2014), Three-dimensional resistivity structure and magma plumbing system of the  
 352 Kirishima Volcanoes as inferred from broadband magnetotelluric data, *Journal of Geophysical*  
 353 *Research: Solid Earth*, 119(1), 198-215, doi:10.1002/2013jb010682.

354 Bagnardi, M., and A. Hooper (2018), Inversion of Surface Deformation Data for Rapid Estimates of  
 355 Source Parameters and Uncertainties: A Bayesian Approach, *Geochemistry, Geophysics, Geosystems*,  
 356 19, doi:10.1029/2018GC007585.

357 Battaglia, M., C. Troise, F. Obrizzo, F. Pingue, and G. De Natale (2006), Evidence for fluid migration as  
 358 the source of deformation at Campi Flegrei caldera (Italy), *Geophysical Research Letters*, 33(1),  
 359 doi:10.1029/2005GL024904.

360 Beauducel, F., A. Peltier, A. Villié, and W. Suryanto (2020), Mechanical Imaging of a Volcano Plumbing  
 361 System From GNSS Unsupervised Modeling, *Geophysical Research Letters*, 47(17),  
 362 e2020GL089419, doi:10.1029/2020GL089419.

363 Brothelande, E., F. Amelung, Z. Yunjun, and S. Wdowinski (2018), Geodetic evidence for  
 364 interconnectivity between Aira and Kirishima magmatic systems, Japan, *Scientific Reports*, 8(1),  
 365 9811, doi:10.1038/s41598-018-28026-4.

366 Chapman N., Apted M., Beavan J., Berryman K., Cloos M., Connor C. et al. (2009), Development of  
 367 Methodologies for the Identification of Volcanic and Tectonic Hazards to Potential HLW Repository  
 368 Sites in Japan: the Kyushu Case Study, in *NUMO-TR-09-02*, edited, Nuclear Waste Management  
 369 Organization of Japan.

370 Chen, C. W., and H. A. Zebker (2001), Two-dimensional phase unwrapping with use of statistical models  
 371 for cost functions in nonlinear optimization, *JOSA A*, 18(2), 338-351,  
 372 doi:10.1364/JOSAA.18.000338.

373 Christiansen, R. L., D. W. Peterson, P. Lipman, and D. Mullineaux (1981), Chronology of the 1980  
 374 eruptive activity, *US Geol. Surv. Prof. Pap*, 1250, 17-30, doi:10.3133/pp1250.

375 Copernicus Climate Change Service (2017): ERA5: Fifth generation of ECMWF atmospheric reanalyses  
 376 of the global climate. *Copernicus Climate Change Service Climate Data Store*, date of access: 3 June  
 377 2019. <https://cds.climate.copernicus.eu/cdsapp#!/home>

378 de Moor, J. M., et al. (2016), Turmoil at Turrialba Volcano (Costa Rica): Degassing and eruptive  
 379 processes inferred from high-frequency gas monitoring, *Journal of Geophysical Research: Solid*  
 380 *Earth*, 121(8), 5761-5775, doi:10.1002/2016jb013150.

381 Fattahi, H., and F. Amelung (2013), DEM Error Correction in InSAR Time Series, *Geoscience and*  
 382 *Remote Sensing, IEEE Transactions on*, 51(7), 4249-4259, doi:10.1109/TGRS.2012.2227761.

- 383 Fattahi, H., M. Simons, and P. Agram (2017), InSAR Time-Series Estimation of the Ionospheric Phase  
 384 Delay: An Extension of the Split Range-Spectrum Technique, *IEEE Transactions on Geoscience and*  
 385 *Remote Sensing*, 55(10), 5984-5996, doi:10.1109/TGRS.2017.2718566.
- 386 Fournier, N., and L. Chardot (2012), Understanding volcano hydrothermal unrest from geodetic  
 387 observations: Insights from numerical modeling and application to White Island volcano, New  
 388 Zealand, *Journal of Geophysical Research: Solid Earth*, 117(B11), doi:10.1029/2012jb009469.
- 389 Germanovich, L. N., and R. P. Lowell (1995), The mechanism of phreatic eruptions, *Journal of*  
 390 *Geophysical Research: Solid Earth*, 100(B5), 8417-8434, doi:10.1029/94jb03096.
- 391 Geshi, N., S. Takarada, M. Tsutsui, T. Mori, and T. Kobayashi (2010), Products of the August 22, 2008  
 392 eruption of Shinmoedake Volcano, Kirishima Volcanic Group, Japan, *BULLETIN OF THE*  
 393 *VOLCANOLOGICAL SOCIETY OF JAPAN*, 55(1), 53-64, doi:10.18940/kazan.55.1\_53 (in Japanese).
- 394 Goldstein, R. M., and C. L. Werner (1998), Radar interferogram filtering for geophysical applications,  
 395 *Geophysical Research Letters*, 25(21), 4035-4038, doi:10.1029/1998GL900033.
- 396 GVP (Global Volcanism Program) (2013). Kirishimayama (282090) in *Volcanoes of the World*, v. 4.9.0  
 397 (04 Jun 2020). Venzke, E (ed.). Smithsonian Institution. Downloaded 17 Aug 2020  
 398 (<https://volcano.si.edu/volcano.cfm?vn=282090>). <https://doi.org/10.5479/si.GVP.VOTW4-2013>
- 399 Hamling, I. J., C. A. Williams, and S. Hreinsdóttir (2016), Depressurization of a hydrothermal system  
 400 following the August and November 2012 Te Maari eruptions of Tongariro, New Zealand,  
 401 *Geophysical Research Letters*, 43(1), 168-175, doi:10.1002/2015gl067264.
- 402 Himematsu, Y., T. Ozawa, and Y. Aoki (2020), Coeruptive and posteruptive crustal deformation  
 403 associated with the 2018 Kusatsu-Shirane phreatic eruption based on PALSAR-2 time series analysis,  
 404 *Earth Planet Sp*, 72(1), 116, doi:10.1186/s40623-020-01247-6.
- 405 Hunter, J. D. (2007), Matplotlib: A 2D Graphics Environment, *Computing in Science & Engineering*,  
 406 9(3), 90-95, doi:10.1109/MCSE.2007.55.
- 407 Imura, R., and T. Kobayashi (1991), Eruptions of Shinmoedake volcano, Kirishima volcano group, in the  
 408 last 300 years, *Bull. Volcanol. Soc. Jpn*, 36, 135-148, doi:10.18940/kazan.36.2\_135 (in Japanese).

- 409 JMA (Japan Meteorological Agency) (2019), 2007-2019 Annual Reports of Volcanic Activity at  
 410 Kirishima, *Volcanic Activity Explanation Material*, [http://www.data.jma.go.jp/svd/vois/data/  
 411 tokyo/STOCK/monthly\\_v-act\\_doc/monthly\\_vact\\_vol.php?id=505](http://www.data.jma.go.jp/svd/vois/data/tokyo/STOCK/monthly_v-act_doc/monthly_vact_vol.php?id=505) (accessed on 29 Jan 2020; in  
 412 Japanese).
- 413 Jolivet, R., R. Grandin, C. Lasserre, M. P. Doin, and G. Peltzer (2011), Systematic InSAR tropospheric  
 414 phase delay corrections from global meteorological reanalysis data, *Geophysical Research Letters*,  
 415 38(17), L17311, doi:10.1029/2011GL048757.
- 416 Jónsson, S., H. Zebker, P. Segall, and F. Amelung (2002), Fault Slip Distribution of the 1999 Mw 7.1  
 417 Hector Mine, California, Earthquake, Estimated from Satellite Radar and GPS Measurements,  
 418 *Bulletin of the Seismological Society of America*, 92(4), 1377-1389, doi:10.1785/0120000922.
- 419 Jung, J., D. j. Kim, M. Lavalley, and S. H. Yun (2016), Coherent Change Detection Using InSAR  
 420 Temporal Decorrelation Model: A Case Study for Volcanic Ash Detection, *IEEE Transactions on  
 421 Geoscience and Remote Sensing*, 54(10), 5765-5775, doi:10.1109/TGRS.2016.2572166.
- 422 Kobayashi, T., Y. Morishita, and H. Munekane (2018), First detection of precursory ground inflation of a  
 423 small phreatic eruption by InSAR, *Earth and Planetary Science Letters*, 491, 244-254,  
 424 doi:10.1016/j.epsl.2018.03.041.
- 425 Lohman, R. B., and M. Simons (2005), Some thoughts on the use of InSAR data to constrain models of  
 426 surface deformation: Noise structure and data downsampling, *Geochemistry, Geophysics,  
 427 Geosystems*, 6(1), doi:10.1029/2004GC000841.
- 428 Lu, Z., T. Masterlark, J. Power, D. Dzurisin, and C. Wicks (2002), Subsidence at Kiska Volcano, Western  
 429 Aleutians, detected by satellite radar interferometry, *Geophysical Research Letters*, 29(18), 2-1-2-4,  
 430 doi:10.1029/2002gl014948.
- 431 Lundgren, P., S. Usai, E. Sansosti, R. Lanari, M. Tesauro, G. Fornaro, and P. Berardino (2001), Modeling  
 432 surface deformation observed with synthetic aperture radar interferometry at Campi Flegrei caldera,  
 433 *Journal of Geophysical Research: Solid Earth*, 106(B9), 19355-19366, doi:10.1029/2001jb000194.

- 434 Manconi, A., T. R. Walter, and F. Amelung (2007), Effects of mechanical layering on volcano  
435 deformation, *Geophysical Journal International*, *170*(2), 952-958, doi:10.1111/j.1365-  
436 246X.2007.03449.x.
- 437 McTigue, D. F. (1987), Elastic stress and deformation near a finite spherical magma body: Resolution of  
438 the point source paradox, *Journal of Geophysical Research: Solid Earth*, *92*(B12), 12931-12940,  
439 doi:10.1029/JB092iB12p12931.
- 440 Miyagi, Y., T. Ozawa, and Y. Kohnno (2013), Crustal Deformation Associated with the 2011 Eruption of  
441 Shinmoe-dake in Kirishima Volcano Group, Southwestern Japan, Detected by DInSAR and GPS  
442 Measurements, *BULLETIN OF THE VOLCANOLOGICAL SOCIETY OF JAPAN*, *58*(2), 341-351,  
443 doi:10.18940/kazan.58.2\_341 (in Japanese).
- 444 Miyagi, Y., T. Ozawa, T. Kozono, and M. Shimada (2014), Long-term lava extrusion after the 2011  
445 Shinmoe-dake eruption detected by DInSAR observations, *Geophysical Research Letters*, *41*(16),  
446 5855-5860, doi:10.1002/2014GL060829.
- 447 Morishita, Y., and T. Kobayashi (2018), Ground Surface Displacement of Kirishima Volcano Group  
448 Detected by ALOS-2 InSAR Time Series Analysis and Effect of Atmospheric Noise Reduction,  
449 *Journal of the Geodetic Society of Japan*, *64*, 28-38, doi:10.11366/sokuchi.64.28 (in Japanese).
- 450 Muffler, L. J. P., D. E. White, and A. H. Truesdell (1971), Hydrothermal Explosion Craters in  
451 Yellowstone National Park, *GSA Bulletin*, *82*(3), 723-740, doi:10.1130/0016-  
452 7606(1971)82[723:Heciyn]2.0.Co;2.
- 453 Nakaboh, M., H. Ono, M. Sako, Y. Sudo, T. Hashimoto, and A. W. Hurst (2003), Continuing deflation by  
454 fumaroles at Kuju Volcano, Japan, *Geophysical Research Letters*, *30*(7), doi:10.1029/2002gl016047.
- 455 Nakada, S., M. Nagai, T. Kaneko, Y. Suzuki, and F. Maeno (2013), The outline of the 2011 eruption at  
456 Shinmoe-dake (Kirishima), Japan, *Earth, Planets, and Space*, *65*, 475-488,  
457 doi:10.5047/eps.2013.03.016.
- 458 Nakamichi, H., Y. Yamanaka, T. Terakawa, S. Horikawa, T. Okuda, and F. Yamazaki (2013), Continuous  
459 long-term array analysis of seismic records observed during the 2011 Shinmoedake eruption activity

460 of Kirishima volcano, southwest Japan, *Earth Planets Space*, 65(6), 551-562,  
 461 doi:10.5047/eps.2013.03.002.

462 Nakao, S., Y. Morita, H. Yakiwara, J. Oikawa, H. Ueda, H. Takahashi, Y. Ohta, T. Matsushima, and M.  
 463 Iguchi (2013), Volume change of the magma reservoir relating to the 2011 Kirishima Shinmoe-dake  
 464 eruption—Charging, discharging and recharging process inferred from GPS measurements, *Earth*  
 465 *Planets Space*, 65(6), 505-515, doi:10.5047/eps.2013.05.017.

466 Narita, S., and M. Murakami (2018), Shallow hydrothermal reservoir inferred from post-eruptive  
 467 deflation at Ontake Volcano as revealed by PALSAR-2 InSAR, *Earth Planet Sp*, 70(1), 191,  
 468 doi:10.1186/s40623-018-0966-6.

469 Narita, S., T. Ozawa, Y. Aoki, M. Shimada, M. Furuya, Y. Takada, and M. Murakami (2020), Precursory  
 470 ground deformation of the 2018 phreatic eruption on Iwo-Yama volcano, revealed by four-  
 471 dimensional joint analysis of airborne and spaceborne InSAR, *Earth Planet Sp*, 72(1), 145,  
 472 doi:10.1186/s40623-020-01280-5.

473 Newhall, C. G., and R. Punongbayan (1996), *Fire and mud: eruptions and lahars of Mount Pinatubo*,  
 474 *Philippines*, Philippine Institute of Volcanology and Seismology Quezon City.

475 Nikkhoo, M., T. R. Walter, P. R. Lundgren, and P. Prats-Iraola (2016), Compound dislocation models  
 476 (CDMs) for volcano deformation analyses, *Geophysical Journal International*, 208(2), 877-894,  
 477 doi:10.1093/gji/ggw427.

478 Ohba, T., K. Nogami, and J.-i. Hirabayashi (1997), Hydrothermal System of the Kirishima Volcanic Area  
 479 Inferred from the Chemical and Isotopic Composition of Spring Waters and Fumarolic Gases,  
 480 *BULLETIN OF THE VOLCANOLOGICAL SOCIETY OF JAPAN*, 42(1), 1-15,  
 481 doi:10.18940/kazan.42.1\_1.

482 Ohba, T., M. Yaguchi, U. Tsunogai, M. Ito, and R. Shingubara (2021), Behavior of magmatic  
 483 components in fumarolic gases related to the 2018 phreatic eruption at Ebinokogen Ioyama volcano,  
 484 Kirishima Volcanic Group, Kyushu, Japan, *Earth Planet Sp*, 73(1), 81, doi:10.1186/s40623-021-  
 485 01405-4.

- 486 Ozawa, T., and T. Kozono (2013), Temporal variation of the Shinmoe-dake crater in the 2011 eruption  
 487 revealed by spaceborne SAR observations, *Earth Planets Space*, *65*(6), 527-537,  
 488 doi:10.5047/eps.2013.05.004.
- 489 Rosen, P. A., E. Gurrola, G. F. Sacco, and H. Zebker (2012), The InSAR scientific computing  
 490 environment, paper presented at EUSAR 2012, 23-26 April 2012.
- 491 Shimono, T., H. Minami, Y. Nishii, H. Ohno, and K. Watanabe (2011), Observation of volcanic crater of  
 492 Mt. Kirishima (Shinmoedake) by airborne SAR, *J Geogr Surv Inst*, *121*, 189-194.
- 493 Stix, J., and J. M. de Moor (2018), Understanding and forecasting phreatic eruptions driven by magmatic  
 494 degassing, *Earth Planet Sp*, *70*(1), 83, doi:10.1186/s40623-018-0855-z.
- 495 Suzuki, Y., M. Nagai, F. Maeno, A. Yasuda, N. Hokanishi, T. Shimano, M. Ichihara, T. Kaneko, and S.  
 496 Nakada (2013), Precursory activity and evolution of the 2011 eruption of Shinmoe-dake in Kirishima  
 497 volcano-insights from ash samples, *Earth, Planets, and Space*, *65*, 591-607,  
 498 doi:10.5047/eps.2013.02.004.
- 499 Tajima, Y., Y. Matsuo, T. Shoji, and T. Kobayashi (2014), Eruptive History of Ebinokogen Volcanic  
 500 Area of Kirishima Volcanoes for the Past 15,000 Years in Kyushu, Japan, *BULLETIN OF THE*  
 501 *VOLCANOLOGICAL SOCIETY OF JAPAN*, *59*(2), 55-75, doi:10.18940/kazan.59.2\_55 (in Japanese).
- 502 Tajima, Y., S. Nakada, F. Maeno, T. Huruzono, M. Takahashi, A. Inamura, T. Matsushima, M. Nagai,  
 503 and J. Funasaki (2020), Shallow Magmatic Hydrothermal Eruption in April 2018 on Ebinokogen  
 504 Ioyama Volcano in Kirishima Volcano Group, Kyushu, Japan, *Geosciences*, *10*(5), 183,  
 505 doi:10.3390/geosciences10050183.
- 506 Takeo, M., Y. Maehara, M. Ichihara, T. Ohminato, R. Kamata, and J. Oikawa (2013), Ground  
 507 deformation cycles in a magma-effusive stage, and sub-Plinian and Vulcanian eruptions at Kirishima  
 508 volcanoes, Japan, *Journal of Geophysical Research: Solid Earth*, *118*(9), 4758-4773,  
 509 doi:10.1002/jgrb.50278.
- 510 Tsukamoto, K., K. Aizawa, K. Chiba, W. Kanda, M. Uyeshima, T. Koyama, M. Utsugi, K. Seki, and T.  
 511 Kishita (2018), Three-Dimensional Resistivity Structure of Iwo-Yama Volcano, Kirishima Volcanic

512       Complex, Japan: Relationship to Shallow Seismicity, Surface Uplift, and a Small Phreatic Eruption,  
513       *Geophysical Research Letters*, *45*(23), 12,821-812,828, doi:10.1029/2018gl080202.

514 Ueda, H., T. Kozono, E. Fujita, Y. Kohno, M. Nagai, Y. Miyagi, and T. Tanada (2013), Crustal  
515       deformation associated with the 2011 Shinmoe-dake eruption as observed by tiltmeters and GPS,  
516       *Earth Planets Space*, *65*(6), 517-525, doi:10.5047/eps.2013.03.001.

517 Wallace, L. M., S. Ellis, K. Miyao, S. Miura, J. Beavan, and J. Goto (2009), Enigmatic, highly active left-  
518       lateral shear zone in southwest Japan explained by aseismic ridge collision, *Geology*, *37*(2), 143-146,  
519       doi:10.1130/G25221A.1.

520 Wessel, P., W. H. Smith, R. Scharroo, J. Luis, and F. Wobbe (2013), Generic mapping tools: improved  
521       version released, *Eos, Transactions American Geophysical Union*, *94*(45), 409-410,  
522       doi:10.1002/2013EO450001.

523 Williams, C. A., and G. Wadge (1998), The effects of topography on magma chamber deformation  
524       models: Application to Mt. Etna and radar interferometry, *Geophysical Research Letters*, *25*(10),  
525       1549-1552, doi:10.1029/98gl01136.

526 Wright, T. J., B. E. Parsons, and Z. Lu (2004), Toward mapping surface deformation in three dimensions  
527       using InSAR, *Geophysical Research Letters*, *31*(1), L01607, doi:10.1029/2003GL018827.

528 Yamazaki, K. i., Y. Yamashita, and S. Komatsu (2020), Vault-housed extensometers recorded a rapid  
529       initial pulse before precursory magma reservoir inflation related to the 2011 eruption of Shinmoe-  
530       dake, Japan, *Earth Planet Sp*, *72*(1), 83, doi:10.1186/s40623-020-01211-4.

531 Yunjun, Z., H. Fattahi, and F. Amelung (2019), Small baseline InSAR time series analysis: Unwrapping  
532       error correction and noise reduction, *Computers & Geosciences*, *133*, 104331,  
533       doi:10.1016/j.cageo.2019.104331.

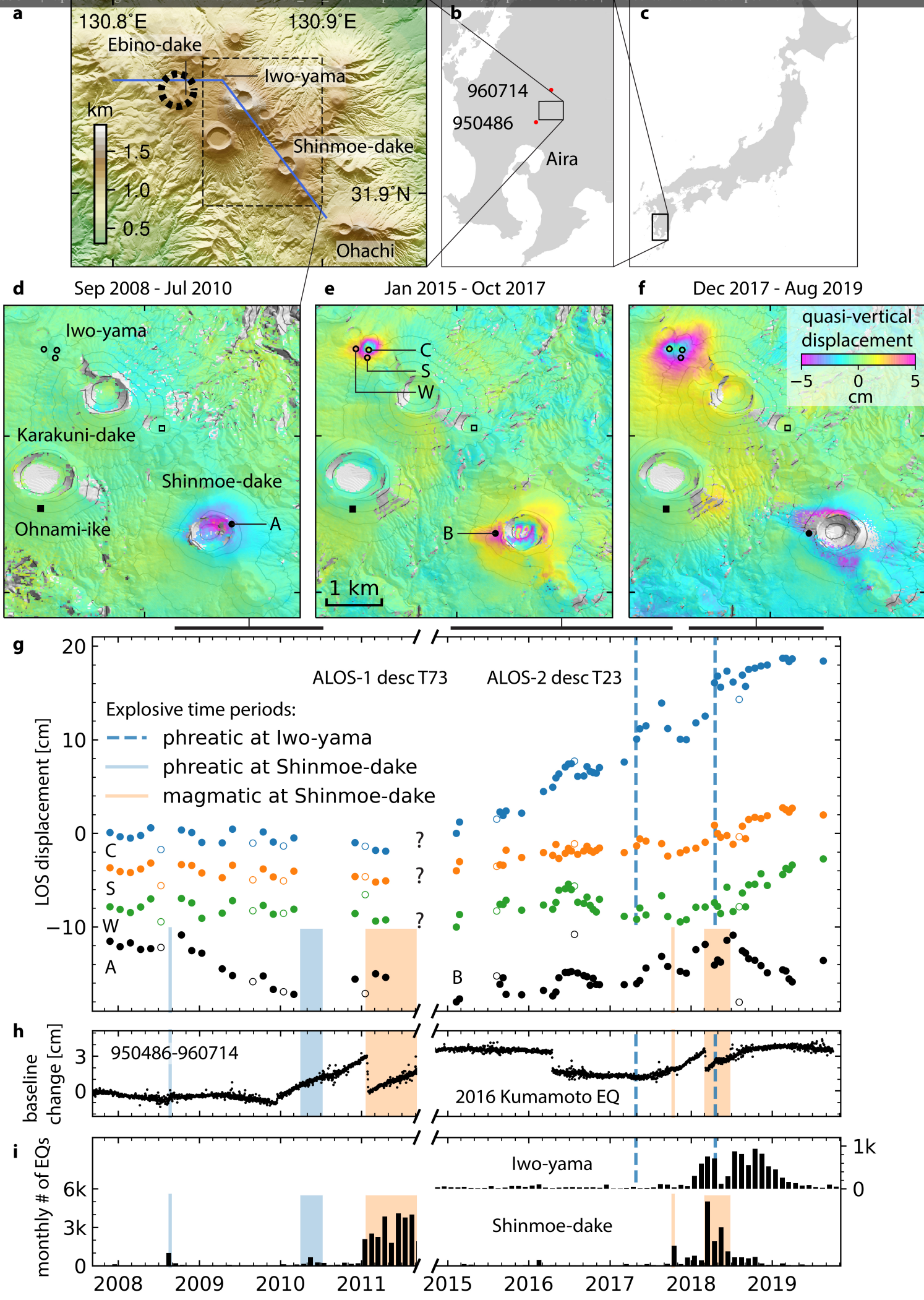
534

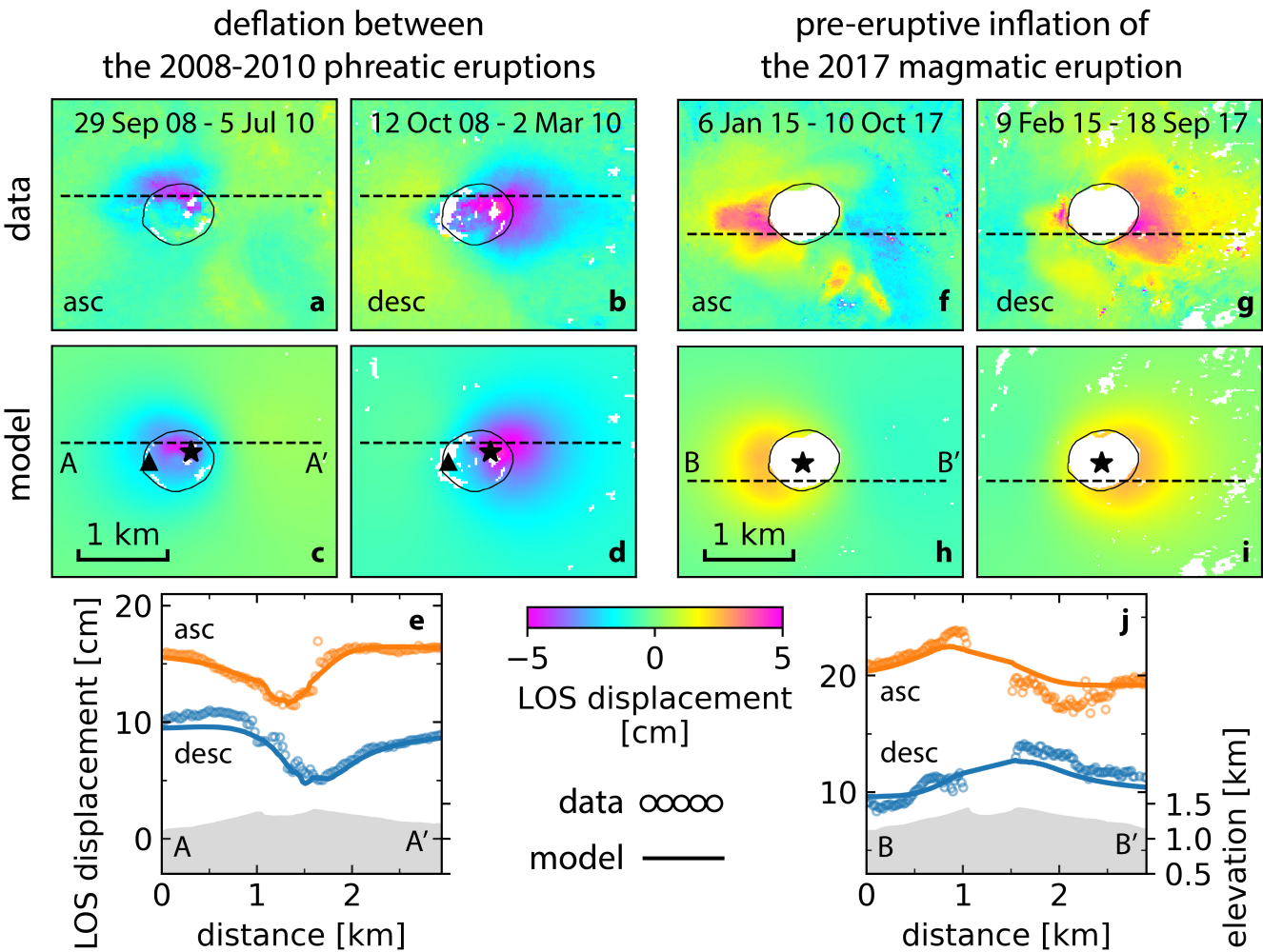
535 **Figure 1.** Geophysical observations at Kirishima during 2008-2019. (a) Geological setting.  
 536 Dashed circle: horizontal location of the deep magmatic source (Nakao et al., 2013). Blue lines:  
 537 cross-section of Fig. 3c. (b-c) Location of Kirishima. Red dots: GPS sites. (d-f) Quasi-vertical  
 538 displacements (d) during the 2008-2010 phreatic eruptions, (e) before and (f) after the 2017  
 539 magmatic eruption. Positive value for uplift. Data are wrapped into  $[-5, 5)$  cm for display. Black  
 540 squares: reference points. Contour lines in every 100 m. (g) Line-of-sight (LOS) displacement  
 541 time-series at Shinmoe-dake and Iwo-yama with respect to the filled and empty black squares,  
 542 respectively (shifted for display). LOS increase for motion toward the satellite. Empty circles:  
 543 noisy acquisitions excluded from the average velocity estimation. (h) Baseline change between  
 544 two GPS stations. (i) Monthly number of earthquakes around Shinmoe-dake and Iwo-yama  
 545 (JMA, 2019).

546  
 547 **Figure 2.** Geodetic modeling results at Shinmoe-dake and Iwo-yama. (a-b) Observed LOS  
 548 displacement at Shinmoe-dake between the 2008-2010 eruptions from ascending and descending  
 549 orbit. (c-d) Prediction for (a-b) from the CDM. Positive value for motion toward the satellite.  
 550 Data are wrapped into  $[-5, 5)$  cm for display. (e) Profile of observed (empty circles) and  
 551 predicted (solid lines) displacement from (a-d) and the topography (gray areas). (f-j) Same as (a-  
 552 e) but for Shinmoe-dake prior to the 2017 eruption. (k-o) and (p-t) Same as (a-e) but for Iwo-  
 553 yama during 2015-2017 with one CDM and during 2017-2019 with two CDMs, respectively.  
 554 Black circles in (a-i): Shinmoe-dake crater rim. Black triangles in (c-d): main vent of the 2008-  
 555 2010 phreatic eruptions (Geshi et al., 2010). Black stars in (c-i): horizontal location of the  
 556 pressure source centroid. Black vertical lines in (o and t): Iwo-yama crater.

557

558 **Figure 3.** Conceptual model of the magmatic and hydrothermal pressure sources at the Kirishima  
559 volcanic complex. (a) Marginal posterior density distributions of depths of pressure source  
560 beneath Shinmoe-dake. From left to right: 1) deflation between the 2008-2010 phreatic  
561 eruptions, 2) inflation-deflation cycles (filled error bar) during the Vulcanian stage in February  
562 2011 (Takeo et al., 2013), 3) deflation (empty error bar) during the 2011-2013 lava extrusion  
563 stage (Miyagi et al., 2014) and 4) inflation before the 2017 magmatic eruption. (b) Same as (a)  
564 but beneath Iwo-yama for inflation before and after December 2017, respectively. (c) Conceptual  
565 model of the plumbing system. The 2008-2010 Shinmoe-dake source has the inferred dimension.  
566 The size of the other sources reflects the ratio of their volume changes and the 2008-2010  
567 Shinmoe-dake volume change, except for the deep magmatic source. The topography is  
568 vertically exaggerated by 25%.  
569





Iwo-yama

